

# Flow Characteristics of a Flat Plate Airfoil Resembling Spinning Samara using PIV

Yogeshwaran G<sup>†</sup> Srisha Rao M V Jagadeesh G

Department of Aerospace Engineering, Indian Institute of Science, Bangalore - 560012

yogeshwarang@iisc.ac.in · srisharao@iisc.ac.in · jaggie@iisc.ac.in

<sup>†</sup>Corresponding author

## Abstract

The single-winged seed, known as a samara, uses autorotation to disperse seeds. The aerodynamic coefficient for the samaras is required for modelling and understanding its performance. Experimental studies using Particle Image Velocimetry (PIV) were conducted in a vertical wind tunnel, examining a flat plate airfoil with  $t/c = 0.1$ , Reynolds numbers of 1218 - 3654, and angles of attack from  $0^\circ$  -  $90^\circ$  similar to samaras. Flow separation occurred at low angles, while moderate angles displayed leading-edge vortex shedding. At high angles, Karman vortex street type of shedding was observed. The computed drag coefficient using control volume analysis aligned with literature, except for specific angles, necessitating further experiments to comprehend variations.

## 1. Introduction

In the technique of natural seed dispersal, the descent velocity of seeds (heavier than air) is the most important factor in determining the dispersal efficiency of the technique (Greene et al.<sup>5</sup>). In order to accomplish this, certain plant groups have adapted a wing-like structure surrounding the seed called samara, that helps in wind dispersal (Norberg<sup>11</sup>). Samaras come in different varieties and are classified according to the flight path, number of wings attached to the seed etc (Yogeshwaran<sup>14</sup>). When a single-winged spinning samara is released from its parent plant, it goes through a phase of random motion called the transition phase before entering a phase called the steady-state, during which it starts to spin around its vertical axis at an angle to the horizontal (conning angle) with a slow descent velocity. Due to the minimal descent velocity resulting from the spinning motion, the samara are effectively carried away by approaching wind gusts and dispersed away from the parent plant. Figure 1 shows the mahogany samara, which can be separated into two areas depending on its mass centre, such as a wing that supports it in the air and a root that carries the seed. A three dimensional scanning of the mahogany samara shows that the cross sectional shapes are thin non standard aerofoils along its span as shown in the figure 2. This three-dimensional structure and physics underlying the steady state motion of the samara are analogous to the autorotative descent of helicopter blades (Norberg<sup>11</sup> & Azuma et al.<sup>2</sup>).



Figure 1: Mahogany samara

The angle of attack distribution over the span for three different natural samaras and for a samara model estimated using steady state kinematic parameters from the mass centre to the wing tip in the literature is shown in figure 3 (Yogeshwaran<sup>14</sup>, Lee et al.<sup>8</sup>, Salcedo et al.<sup>12</sup>, Azuma et al.<sup>2</sup> & Yogeshwaran et al.<sup>15</sup>). The operating angle of attack regime for the single winged spinning samaras are in the range of  $20^\circ$  at the wing tip to maximum of  $90^\circ$  at its root. Their corresponding Reynolds number calculated based on the mean chord and descent velocity of the samara is found to operate in the range of 897 to 3474 with aspect ratio from 2 to 4. The flow separates along the leading edge in the wing region due to the thin cross sectional shape (figure 2), high operating angle of attack, and moderate operating

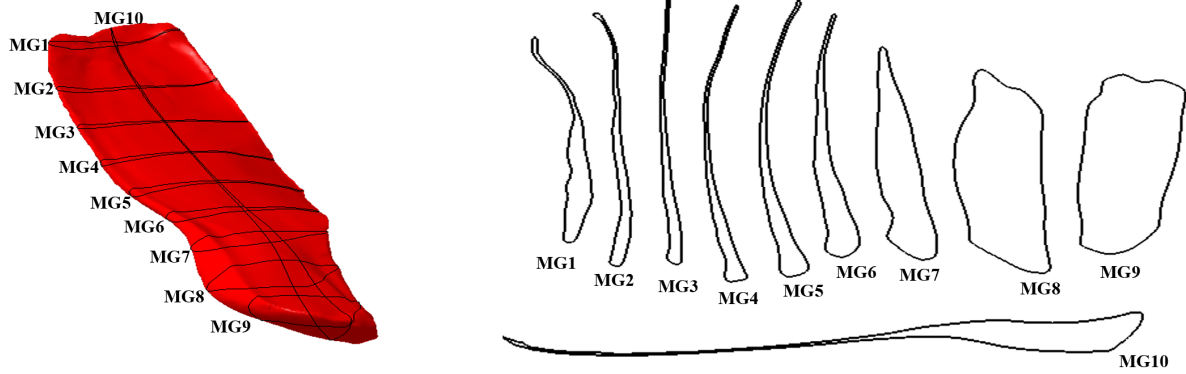


Figure 2: Cross sectional view - Mahogany samara

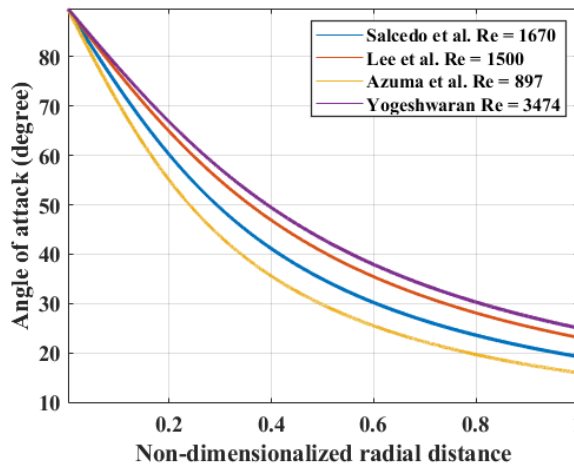


Figure 3: Angle of attack distribution across the span different samaras and models from the literature

Reynolds number. Due to the spinning motion of the samara, the separated flow reattached along the chord and created a stable Leading Edge vortex (LEV), then shed into the wingtip vortex at the wing tip (Lentink et al.<sup>9</sup>, Lentink et al.<sup>10</sup> & Yogeshwaran et al.<sup>4</sup>). The LEV not only prevents a loss of lift and an increase in drag that would otherwise be caused by flow separation, but it also causes the local lift coefficient along the span to achieve its highest possible value of 5 (Lentink et al.<sup>9</sup>). It was found that the formation of LEV was the key to understanding the extraordinary flight performance of the spinning samaras, which is similar to the behaviour of other biological flyers such as birds (Ellington et al.<sup>3</sup>), insects, and bats, etc., as other instances.

Based on the theory of rigid body mechanics, the governing equation of motion for spinning samaras with mass-centered reference frames, assuming that the samara stays rigid during its transition and steady state, is given as (Arranz et al.<sup>1</sup>),

$$m\dot{\vec{u}}_g = \vec{F}_{exG} \quad (1)$$

$$I_G\dot{\vec{\Omega}} + \vec{\Omega} \times I_G\vec{\Omega} = \vec{M}_{exG} \quad (2)$$

There are two distinct approaches that can be used to determine the aerodynamic external forces and moments that are acting on the spinning samaras. First, a Direct Numerical Simulation (DNS) of the complete incompressible Navier-Stokes equation can be solved to obtain the pressure and shear stress acting on the surface of the samara (Arranz et al.<sup>1</sup> & Lee et al.<sup>7</sup>). Second, performance of the spinning samaras in steady state can be evaluated using a Blade Element Momentum Theory (BEMT) similar to the way helicopter blade performance is calculated (Azuma et al.<sup>2</sup> & Norberg<sup>11</sup>). In the BEMT, the aerodynamic forces and moments that are acting at a cross section are evaluated,

and then integrated along the span, in order to obtain the resultant force and moments. Equations 3 and 4 show the expression for the resulting force and moments ( $Q$ ) under the assumption that the weight of the samara is balanced by its upward thrust and that the resultant torque is zero. In order for these equations to be accurately solved, the aerodynamic coefficient as a function of angle of attack corresponding to the Reynolds number of the spinning samaras that incorporates the influence of LEV needs to be provided.

$$m \cdot g = \int (dL \cdot \cos \beta + dD \cdot \sin \beta) dr \quad (3)$$

$$Q = \int (dL \cdot \sin \beta - dD \cdot \cos \beta) \cdot r \cdot dr = 0 \quad (4)$$

The BEMT is commonly utilised to find the relationship among the geometric and the steady state parameters. For designing engineering samara, BEMT theories provide quick results but require aerodynamic coefficient as a function of wide angle of attack range at these low Reynolds numbers. The aerodynamic coefficient values have a significant influence in determining its performance, as illustrated in equations 3 and 4. So far, there hasn't been much work done to figure out the sectional lift, drag, and moment coefficients for spinning samaras or other similar flight regimes. The lift calculation derived from the sectional circulation strength of the PIV experiments and DNS results serves as the basis for calculating the lift coefficient (Lee et al.<sup>7</sup> & Lentink et al.<sup>9</sup>). A substantial work has been made recently by Jung et al.<sup>6</sup> to determine the lift coefficient as function of angle of attack for the samara flight. They used the theories of normal force model and Polhamus leading edge suction analogy that were used to determine the aerodynamic coefficient of insect flight of similar Reynolds number regime. They showed that the normal force model with correction to angle of attack from the induced velocity distribution, was able to predict the trend of lift coefficient similar to the experimentally observed with variable zero lift coefficient. This is one of the pioneering work in determining the sectional lift coefficient for samara flight.

It is unsure whether the evaluated lift coefficient from the normal force model can be applied to any samara or samara models with a distinct geometry. On the other hand, the value of drag and moment coefficient of the samara is yet to be explored. Unlike lift force, determination of sectional drag force from velocity field of PIV is not clear due to spinning motion of the samara. Additionally, the values of the drag coefficient for even a flat plate aerofoil at these Reynolds numbers for the range of angle of attack are not available in the literature (Winslow et al.<sup>13</sup>). The objective of the present study is to use PIV in the vertical wind tunnel to calculate the drag coefficient values from the flow over the flat plate aerofoil in the Reynolds number regime resembling samaras for angle of attack ranging from  $0^\circ$  to  $90^\circ$ . The drag force acting on it is determined from the obtained velocity field using the wake deficit method. This research contributes to our understanding of the fundamental flow physics over a flat plate at moderate Reynolds for a wider angle of angle attack.

## 2. Experimental Methodology

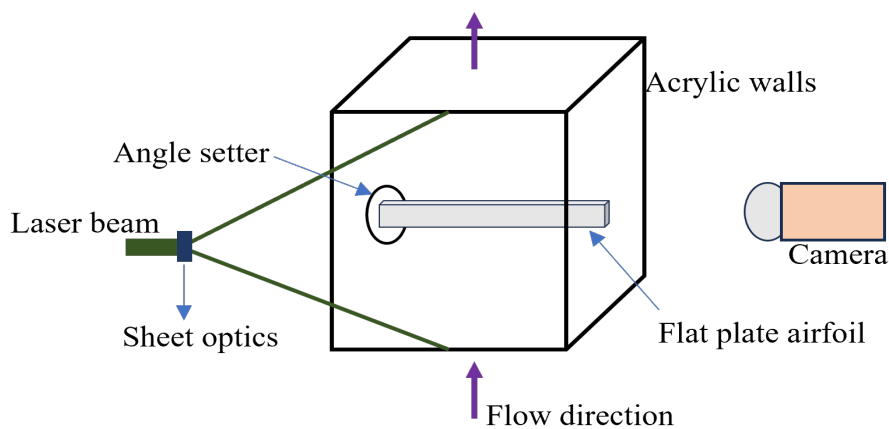


Figure 4: Schematic of the experimental setup

The PIV experimental study on flat plate aerofoil is being carried out in the vertical wind tunnel that was designed and developed in our laboratory. The vertical wind tunnel is fitted with a fan section at the bottom end and connected

## SHORT PAPER TITLE

to a vertical inlet section measuring  $350 \text{ mm} \times 350 \text{ mm}$ . The honeycomb and screens section, is connected to the inlet section and then it is connected to the test section of the vertical wind tunnel. The cross-sectional sizes and forms of all of these portions remained constant. The test section of the wind tunnel has dimensions of  $350 \text{ mm} \times 350 \text{ mm}$  and a length of  $400 \text{ mm}$ . A vertical uniform flow is created inside the test section as the fan at the lower end forces air vertically upward inside the duct as shown in figure 4. The voltage regulator is used to adjust the test sectional velocity, and the walls of the test section are made of acrylic. The flat plate aerofoil, which is made of acrylic and measures  $350 \text{ mm}$  in length and  $30 \text{ mm}$  in chord ( $C$ ), is positioned inside the test section, with both of its side edges held to the walls on each side of the test section. It was chosen that the Reynolds number of the flat plate would be 1218, 2436 and 3654 and the thickness to chord ratio was to be 0.1, with test sectional velocities being set at  $0.6 \text{ m/s}$  to  $1.8 \text{ m/s}$ . The angle of attack ( $\varphi$ ) of the flat plate aerofoil was adjusted from  $0^\circ$  to  $90^\circ$  using an angle setter as shown in figure 4 .

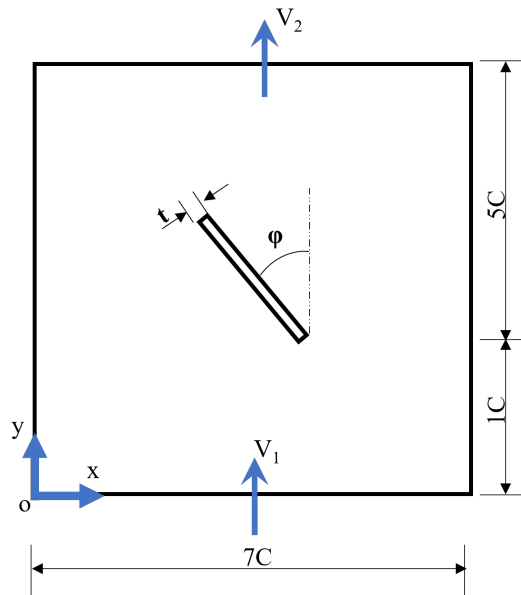


Figure 5: Chosen field of view for control volume analysis

A double-pulsed NdYAG laser (BeamTech Vlite-135) with wavelength of  $532 \text{ nm}$  that was available in our laboratory is used for the PIV experiments. The laser beam with a diameter of  $0.7 \text{ cm}$  is formed into a laser sheet and passed through the centre of the test section. Using the high-speed controller (LaVision), the laser beam is synchronized with the phantom Miro 110 camera recording in PIV mode. The laser is operated at its maximum frequency of  $15 \text{ Hz}$  with a pulse width of  $8 \text{ ns}$ . The duration between frames is maintained at  $600 \text{ ms}$ , and the energy of the laser is kept at  $100 \text{ mJ}$ . The camera was fitted with a  $50 \text{ mm}$  Nikon AF lens, and its resolution is set at  $896 \times 800$  pixels capturing the required field of view. The test section is seeded from the inlet of the fan section of the vertical wind tunnel using an Antari 5600 smoke flow generator, which produces smoke particles. The Davis 8 software from LaVision was utilised as the interface between the high speed controller, laser beam, and camera for capturing and processing the images. The triggering of the entire system is done manually. The left most corner of the field of view is chosen as origin of the Cartesian coordinate system with Y-axis pointing upwards as shown in figure 5. The captured image pairs were processed using adaptive cross correlation algorithm in the Davis software. The interrogation window size of  $64 \times 64$  pixels and a search window size of  $512 \times 512$  pixels with a  $87\%$  overlap in both directions was used.

### 3. Results

Figure 6 depicts a typical raw images of a flat plate with an angle of attack varying from  $0^\circ$  to  $90^\circ$  within the test chamber of a vertical wind tunnel. The camera is mounted above the centre of the flat plate, which results in a black region occupying the flat plate at all angles of attack. The size of this dark region is dependent on the angle of attack. The transparent acrylic flat plate permits the laser beam to travel through it and enables us to see the flow on the bottom surface at lower angles of attack, while at higher angles of attack, it casts a minimal shadow. The velocity contours non-dimensionalized with the upstream velocity of the test section with the velocity arrows for three different Reynolds numbers for the whole angle of attack regime are shown in figures 7, 8 and 9 . In the vector field plots, the area occupied by the flat plate is depicted as a black region because it was masked out during image processing. The

vorticity field for the two different instances for  $Re = 1281$  at an angle of attack of  $90^\circ$  is illustrated in figure 14, which exhibits the phenomenon of vortex shedding. The time-averaged y-component velocity that was calculated at the exit of the control volume (figure 5) for  $Re=1218$  each of the different angles of attack is depicted in figure 11.

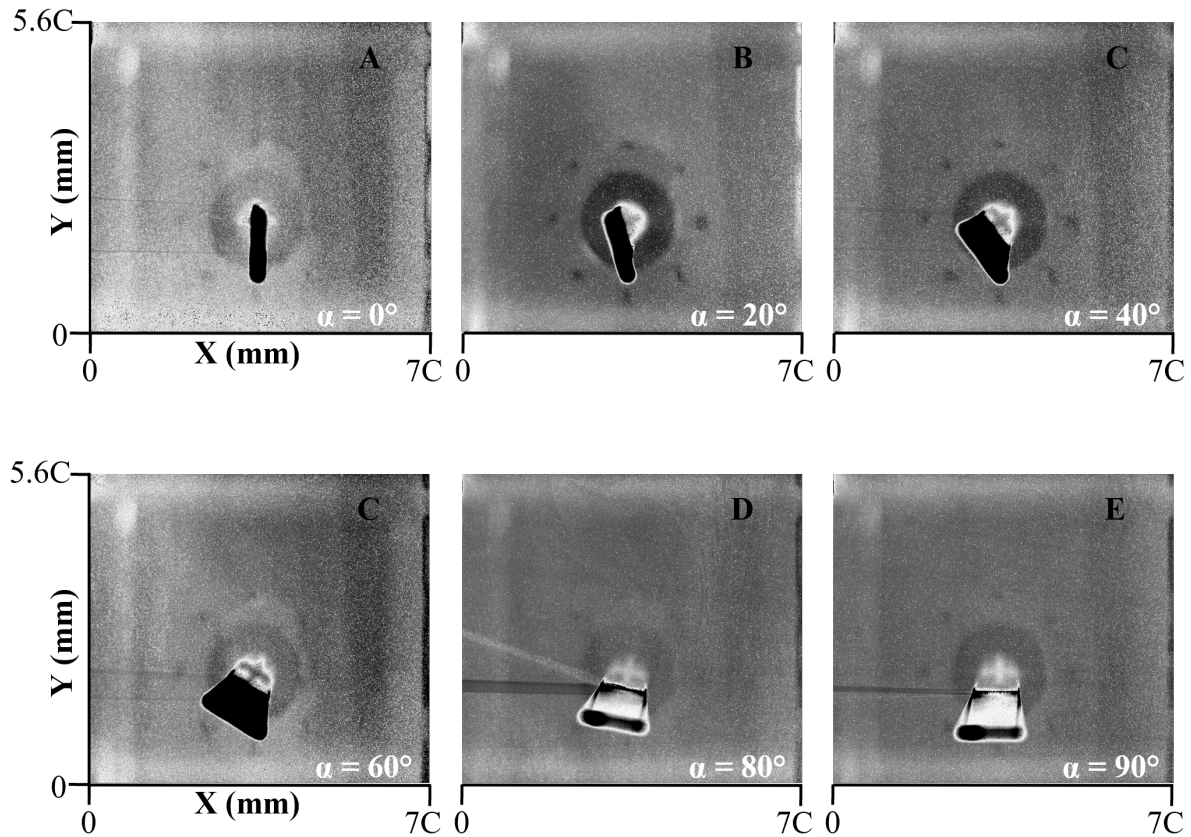


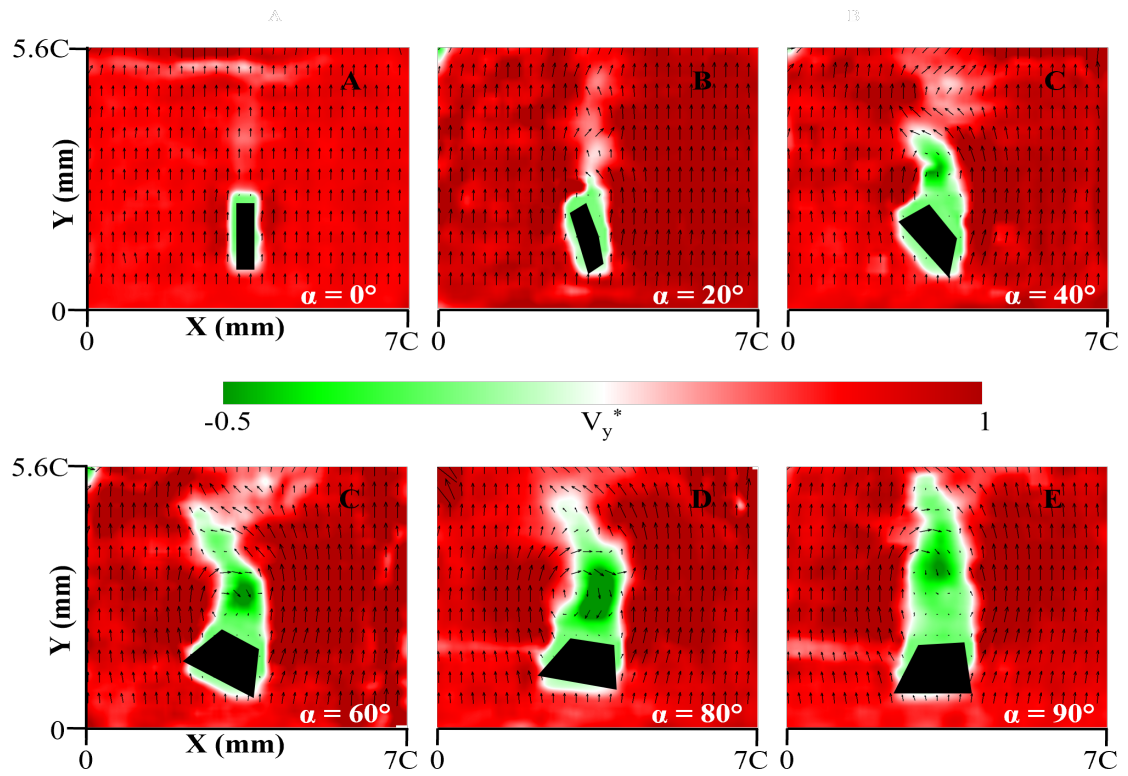
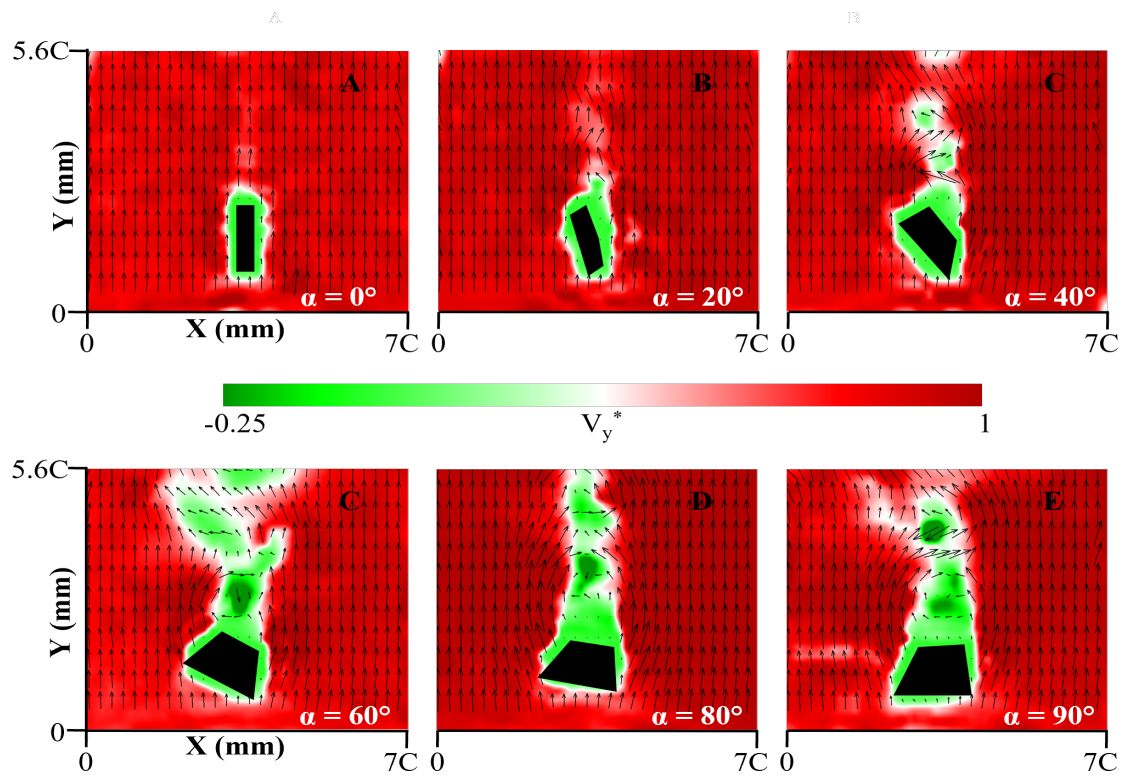
Figure 6: Raw image of the flat plate at angle of attack from  $0^\circ$  to  $90^\circ$

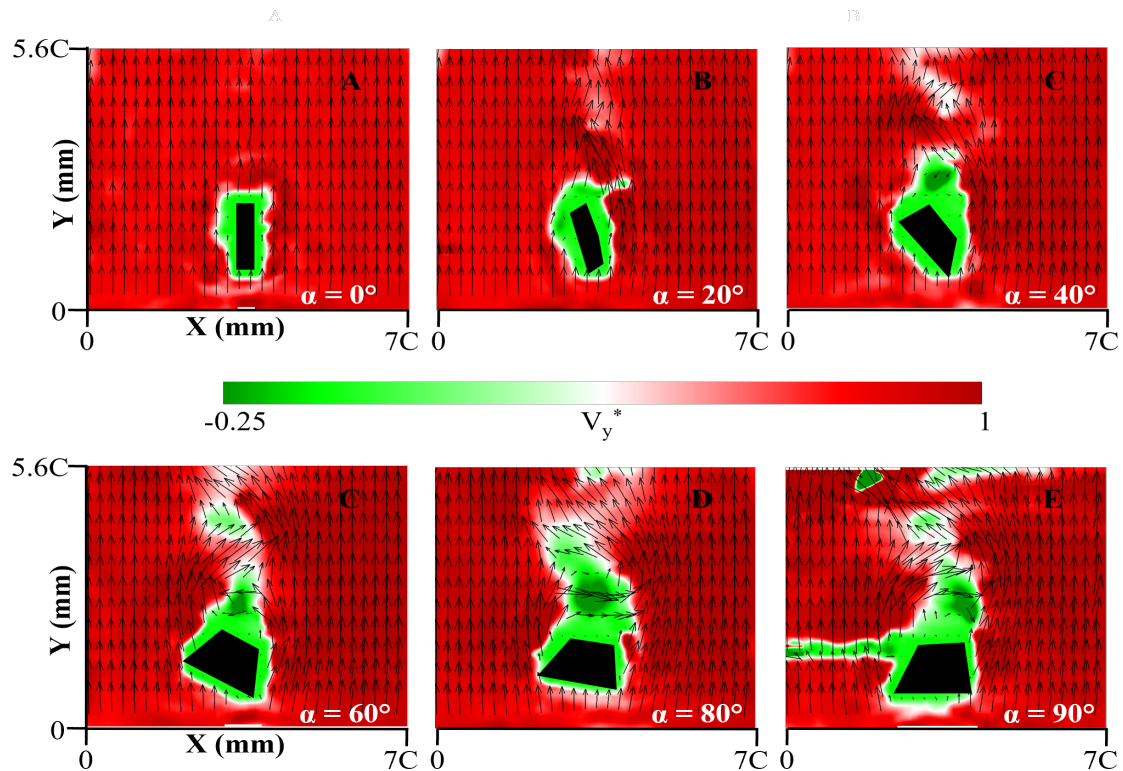
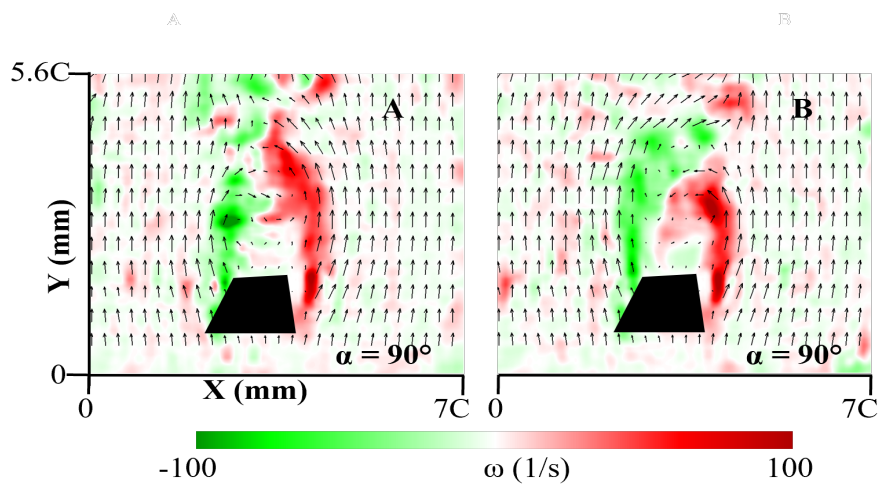
#### 4. Discussions

The velocity field around the flat plate aerofoil can be examined by separating it into four regions: upstream, windward, leeward, and downstream (wake). As the flow gets closer to the leading edge of the aerofoil, as is well-known, the upstream region experiences a small reduction in the velocity. This can be observed for all of the cases as close to the leading edge of the flat plate aerofoil. To ensure mass conservation, the flow over the flat plate aerofoil accelerated on the windward side and decelerated proportionately on the leeward side. The change in the velocity field results in an adverse pressure gradient on the leeward side and a favourable pressure gradient on the windward side, with the exception of angles of  $0^\circ$  and  $90^\circ$ , since the geometry is symmetric with respect to the upstream flow.

For the chosen the angle of attack and Reynolds number, the flow remains attached in the windward side till the trailing edge. Despite the considerable thickness of the aerofoil at  $0^\circ$  angle of attack and in the chosen the Reynolds number regime, the flow remains attached on both sides of the flat plate. For angles other than  $0^\circ$ , the adverse pressure gradient on the leeward with sharp leading edge causes the flow to separate along its chord. Even though we have a complete velocity field from the PIV approach, the velocity value close to the flat plate is obscured by laser beam reflections. Because of this, it is difficult for us to determine the exact site of separation. But from the velocity field at the flat plate region indicates that it either separates at the top leading edge or in the region nearby along the chord.

For  $Re=1000$  at an AOA of  $20^\circ$ , the separated flow seems to not reconnect along the chord and causes a lot of fluctuations in its wake region. When the angle is more than  $20^\circ$  to  $80^\circ$  at  $Re = 1218$ , a vortex forms on the leeward side, close to the plate, and sheds into the wake region. The wake of the flow starts to shed like a von Karman vortex street for  $Re = 1218$  and an AOA of  $90^\circ$ . Figure 10 (A,B) shows their corresponding vorticity field at two separate instances, illustrating the formation of clockwise and anticlockwise vortex clearly shows the von Karman vortex street.

Figure 7: Velocity field around flat plate aerofoil at  $Re = 1218$ Figure 8: Velocity field around flat plate aerofoil at  $Re = 2436$

Figure 9: Velocity field around flat plate aerofoil at  $Re = 3654$ Figure 10: Vorticity field around flat plate aerofoil at two different time instances at  $Re = 1218$  &  $AOA = 90^\circ$ 

The shear layer divides the wake core from the outer flow region and can be seen as a white line in the velocity field for all angles of attack and Reynolds numbers. On the leeward side, close to the flat plate, in the region of the re-circulation zone, the y-component of the plate reaches its minimal value. In the various angles of attack regimes with varying Reynolds numbers, similar flow phenomena can be observed.

As expected, it is found that the region of the wake core expands in relation to the angle of attack. This is in accordance with the time averaged velocity profile obtained at various angles of attack, where the descending velocity reaches its lowest point at the largest angle of attack and vice versa (figure 11). Additionally, the Y-component velocity increases outside the wake core region at the exit plane. Assuming that the far field pressure is equal to the ambient pressure because of the distance (5C) that was used to determine exit velocity, it is possible to compute the drag force acting on the flat plate using the reduction of momentum flux in the Y-direction. The control volume is chosen as

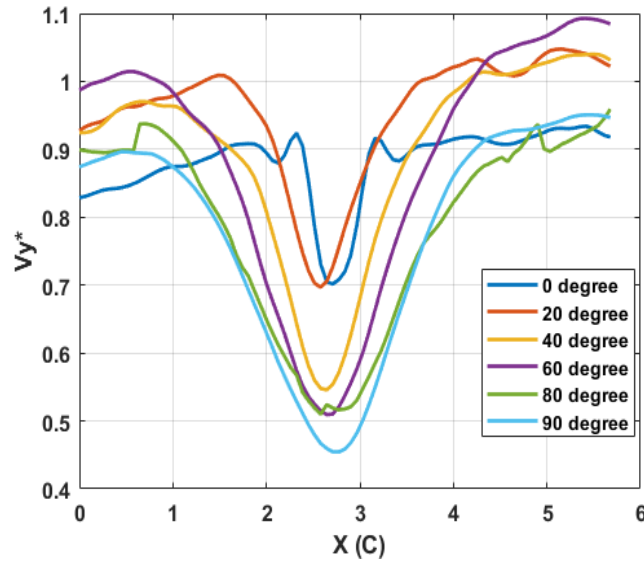


Figure 11: Time averaged exit velocity profiles at different angle of attack for Re=1218

shown in figure 9, and the expression for calculating the drag force and coefficient of drag is given equation 6 and 7. Because the results of the investigation showed that the velocity field on the side region of the control volume was uniform, the drag force could be computed by taking into account only the mean exit velocity and the test sectional velocity. The values of the drag coefficient were found to range from 0.05 to 3, which is a range that is comparable to the one obtained in Jung et al.<sup>6</sup> But for an angle of 20°, the value of the drag coefficient was found to have a negative value, which was found to be inconsistent with the physics of actual flow. Additional experiments have to be carried out in order to comprehend the rationale for the unreasonable value of the drag coefficients.

$$D = \rho \cdot \int_0^{6c} (V_1^2 - V_2^2) \cdot dy \quad (5)$$

$$Cd = \frac{0.5 \cdot D}{\rho \cdot C \cdot V_1^2} \quad (6)$$

## 5. Conclusions

To understand the drag coefficient of the samara type flight, an experimental PIV study flow over a flat plate aerofoil with  $t/c = 0.1$  is carried out in the vertical wind tunnel over the Reynolds number regime of 1000 to 3000 and angle of attack of 0° to 90°. Even at low angles of attack, the flow begins to separate from its leading edge, and at moderate angles of attack, vortex shedding is observable. Irrespective of the chosen Reynolds number, the flow begins to shed like a Karman vortex street at very high angles of attack. To estimate the drag force and drag coefficient from the acquired velocity field, a control volume analysis approach was used. The drag coefficient value that was computed is comparable to that which was found in the currently available literature, with an unrealistic value for at specific angles of attack. To completely comprehend the variation in drag coefficient as a function of angle of attack, including effects of pressure force at the exit plane of the control volume, additional experiments must be carried out.

## 6. Acknowledgments

The authors would like to express their gratitude to the Indian Institute of Science, Bangalore for providing the necessary resources for this research endeavor. The valuable assistance and support of the members of the LHSR in conducting the experiments are greatly acknowledged. The authors also extend their appreciation to the interns, Mr. Shubhanga Amardeep, Mr. Vishwanath Nagaraj, Mr. Tarun Sosale, and Mr. Darshan from PES University, for their contributions in constructing the vertical wind tunnel used in the study.

## References

- [1] G. Arranz, M. Moriche, M. Uhlmann, O. Flores, and M. García-Villalba. Kinematics and dynamics of the auto-rotation of a model winged seed. *Bioinspiration and Biomimetics*, 13(3), 2018.
- [2] Akira Azuma and Kunio Yasuda. Flight performance of rotary seeds. *Journal of Theoretical Biology*, 138(1):23–53, 1989.
- [3] C P Ellington, C Van den Berg, and A P Willmott. Leading-edge vortices in insect flight. *Nature*, 384(December):626–630, 1990.
- [4] Yogeshwaran G, Srisha Rao M.V., and Jagadeesh Gopalan. Investigation of wake flow around the single-winged autorotating seed using PIV. *AIAA SciTech Forum*, (January):1–9, 2023.
- [5] D F Greene and E a Johnson. Seed mass and dispersal capacity in wind-dispersal diaspores. *Oikos*, 67(1):69–74, 1993.
- [6] Byung Kwon Jung and Djamel Rezgui. Sectional Leading Edge Vortex Lift and Drag Coefficients of Autorotating Samaras. *Aerospace*, 10(5):1–32, 2023.
- [7] Injae Lee and Haecheon Choi. Scaling law for the lift force of autorotating falling seeds at terminal velocity. *Journal of Fluid Mechanics*, 835:406–420, 2018.
- [8] Sang Joon Lee, Eui Jae Lee, and Myong Hwan Sohn. Mechanism of autorotation flight of maple samaras (*Acer palmatum*). *Experiments in Fluids*, 55(4), 2014.
- [9] D. Lentink, W. B. Dickson, J. L. van Leeuwen, and M. H. Dickinson. Leading-Edge Vortices Elevate Lift of Autorotating Plant Seeds. *Science*, 324(5933):1438–1440, 2009.
- [10] David Lentink and Michael H. Dickinson. Rotational accelerations stabilize leading edge vortices on revolving fly wings. *Journal of experimental biology*, 212(Pt 16):2705–2719, 2009.
- [11] R. ÅKE NORBERG. Autorotation, Self-Stability, and Structure of Single-Winged Fruits and Seeds (Samaras) With Comparative Remarks on Animal Flight. *Biological Reviews*, 48(4):561–596, 1973.
- [12] E Salcedo, C Treviño, R O Vargas, and L Martínez-Suástegui. Stereoscopic particle image velocimetry measurements of the three-dimensional flow field of a descending autorotating mahogany seed (*Swietenia macrophylla*). *The Journal of experimental biology*, 216(Pt 11):2017–30, 2013.
- [13] Justin Winslow, Hikaru Otsuka, Bharath Govindarajan, and Inderjit Chopra. Basic Understanding of Airfoil Characteristics at Low Reynolds Numbers (104â105). *Journal of Aircraft*, 55(3):1050–1061, 2017.
- [14] G Yogeshwaran. On Flow Physics of Spinning Samaras. *M.Sc Thesis, Indian Institute of Science Bangalore*, (July), 2018.
- [15] G Yogeshwaran, M. V.Srisha Rao, and Jagadeesh Gopalan. Aerodynamics and Design of Spinning Samara Model. In *Proceedings of 16th Asian Congress of Fluid Mechanics. Lecture Notes in Mechanical Engineering. Springer, Singapore.*, number December, pages 51–57, 2021.